Fusion and quasifission studies for the ^{40}Ca + ^{186}W, ^{192}Os reactions

E. Prasad,[*] D. J. Hinde, E. Williams, M. Dasgupta, I. P. Carter, K. J. Cook, D. Y. Jeung, D. H. Luong, C. S. Palshetkar,[†]
D. C. Rafferty, K. Ramachandran,[†] C. Simenel, and A. Wakhle[‡]

Department of Nuclear Physics, Research School of Physical Sciences and Engineering, Australian National University, Canberra,
Australian Capital Territory 2601, Australia

(Received 7 June 2017; published 14 September 2017)

Background: All elements above atomic number 113 have been synthesized using hot fusion reactions with calcium beams on statically deformed actinide target nuclei. Quasifission and fusion-fission are the two major mechanisms responsible for the very low production cross sections of superheavy elements.

Purpose: To achieve a quantitative measurement of capture and quasifission characteristics as a function of beam energy in reactions forming heavy compound systems using calcium beams as projectiles.

Methods: Fission fragment mass-angle distributions were measured for the two reactions ^{40}Ca+^{186}W and ^{40}C+^{192}Os, populating ^{226}Pu and ^{232}Cm compound nuclei, respectively, using the Heavy Ion Accelerator Facility and CUBE spectrometer at the Australian National University. Mass ratio distributions, angular distributions, and total fission cross sections were obtained from the experimental data. Simulations to match the features of the experimental mass-angle distributions were performed using a classical phenomenological approach.

Results: Both ^{40}Ca+^{186}W and ^{40}C+^{192}Os reactions show strong mass-angle correlations at all energies measured. A maximum fusion probability of $60-70\%$ is estimated for the two reactions in the energy range of the present study. Coupled-channels calculations assuming standard Woods-Saxon potential parameters overpredict the capture cross sections. Large nuclear potential diffuseness parameters ~ 1.5 fm are required to fit the total capture cross sections. The presence of a weak mass-asymmetric quasifission component attributed to the higher angular momentum events can be reproduced with a shorter average sticking time but longer mass-equilibration time constant.

Conclusions: The deduced above-barrier capture cross sections suggest that the dissipative processes are already occurring outside the capture barrier. The mass-angle correlations indicate that a compact shape is not achieved for deformation aligned collisions with lower capture barriers. The average sticking time of fast quasifission events is 10^{-20} s.

I. INTRODUCTION

Superheavy elements (SHEs) exist solely due to the microscopic stabilization resulting from nuclear shell effects; as a result, they offer an extreme test of our understanding of nuclear physics. The synthesis of SHEs and investigation of their properties are among the most challenging research topics in science, owing to the very low production cross sections of the SHEs, often of the order of a pico barn or less.

The production of a SHE is generally considered to follow a sequence of three processes: the capture of the projectile and target, formation of the completely equilibrated compound nucleus (CN), and the survival of the CN against fission decay resulting in an evaporation residue (ER). Hence, the ER formation cross section may be treated as the product of the capture cross section (σ_{cap}), CN formation probability (P_{CN}), and survival probability (W_{sur}) of the CN against fission.

The outcome of the first stage—capture—has two competing components: fusion and quasifission [1–4]. Quasifission is partly responsible for the very low production cross sections of SHEs because in quasifission, the system reseparates soon after capture, before reaching the CN configuration. It thus suppresses fusion and the ER cross sections.

Quasifission is a dynamical nonequilibrium process which is heavily influenced by entrance channel properties such as beam energy [5–7] and entrance channel mass asymmetry [8–10], and nuclear structure effects such as static deformation [7,11,12], shell closure [13,14], and isospin [13]. Even though quasifission has very high cross sections in reactions involving heavy nuclei, a complete understanding of this process is marred by both the significant overlap of quasifission and fusion-fission observables and the complex dependence of quasifission on various entrance channel variables. Knowing that quasifission and fusion-fission are the most significant processes determining P_{CN} and W_{sur}, understanding the competition between these processes is essential for making reliable predictions of the best reactions to form new superheavy elements and isotopes.

Both cold [15,16] and hot [17–19] fusion reactions have been employed for the synthesis of SHEs. Elements between $Z = 107-113$ have been produced using cold fusion reactions where target nuclei of ^{208}Pb or ^{209}Bi were collided with massive projectiles [16]. Elements beyond $Z = 113$ were

---

[*]Permanent address: Department of Physics, School of Mathematical and Physical Sciences, Central University of Kerala, Kasaragod 671314, India; prasadcukerala@gmail.com

[†]Present address: Nuclear Physics Division, Bhabha Atomic Research Centre, Mumbai 400085, India.

[‡]Present Address: National Superconducting Cyclotron Laboratory, Michigan State University, Michigan 48824, USA.

produced through hot fusion reactions with actinide nuclei as targets. The lower Coulomb product ($Z_P Z_T$, where Z_P and Z_T are the atomic numbers of the projectile and target nuclei, respectively) and the more neutron-rich CN produced in hot fusion reactions compared with cold fusion favor a higher fusion probability in the former case. The most neutron-rich isotope of calcium (^{48}Ca) has been used as the projectile in most of these measurements [19]. In this context, a series of measurements is being carried out at the Australian National University (ANU) to study fusion-fission and quasifission processes in reactions using different isotopes of Ca (^{40}Ca and ^{48}Ca) as the projectiles with targets ranging from ^{142}Nd [20] to ^{249}Cf. The results from the measurements of ^{40}Ca with deformed ^{186}W and ^{192}Os target nuclei are presented and discussed in this paper.

The paper is organized as follows: The experimental details are presented in Sec. II; the data analysis and results on mass ratio distributions and angular distributions are given in Sec. III; Sec. IV presents a detailed description of classical simulations performed to reproduce the experimental mass-angle distributions and calculated average time scales of fast quasifission; and finally, the work is summarized in Sec. V.

II. EXPERIMENTAL DETAILS

The measurements were performed at the Heavy Ion Accelerator Facility of the ANU. Pulsed ^{40}Ca beams with a pulse separation of 107 ns and FWHM of 0.7–1.5 ns from the 14UD Pelletron accelerator were boosted in energy using the superconducting linear accelerator. Isotopically enriched ^{186}W (94 μg/cm^2 on 40 μg/cm^2 carbon) and ^{192}Os (100 μg/cm^2 on 20 μg/cm^2 carbon) targets were used in the experiments, with carbon backings facing downstream in both cases. The experiments were performed at laboratory energies (after correcting for energy loss in the target assuming that the interactions occurred at the center of the target) of 199.3, 204.3, 214.3, and 225.4 MeV for the ^{40}Ca+^{186}W reaction and 199.3, 204.3, 214.3, 225.3, 239.8, and 262.6 MeV for the ^{40}Ca+^{192}Os reaction. The target normal was oriented 60° to the beam axis in both cases, which reduced the energy loss of the fission fragments in the target and avoided shadowing of the detectors by the target ladder. The reaction products were detected using the CUBE spectrometer [11].

The CUBE detector setup consists of two large-area position-sensitive multiwire proportional counters (MWPCs), each having an illuminated area of 279 × 357 mm^2. These detectors were mounted at 45° (front detector) and 90° (back detector) scattering angles with respect to the beam direction. The normal to the detector central foils were 180 mm from the target center at azimuthal angles of 180° and 0° for the back and front detectors, respectively. In this configuration, both these detectors had a large angular acceptance of 75º ranging from 5° to 80° (front detector at $\theta_2 = 45°$) and 50° to 125° (back detector at $\theta_1 = 90°$). The gas detectors provided X and Y position information for detected particles through delay line readouts, with a typical resolution of about 1 mm. In addition to the position information, these detectors also provided timing and energy-loss signals for each particle reaching the detectors. The fast timing information was obtained from the cathode

foil of each detector, and was measured with respect to the beam pulse. Two silicon detectors were mounted at $\theta = 23°$ at azimuthal angles of 90° and 270° to measure the Rutherford scattered events. These Rutherford events were used for the absolute cross section normalization.

Using the same CUBE configuration, we also measured the elastic scattering for the ^{50}Cr+^{184}W reaction at a laboratory beam energy of 185.3 MeV. For this measurement, a pulsed ^{50}Cr beam from the accelerator was used to bombard a 64 μg/cm^2 thick ^{184}W target on a 40 μg/cm^2 thick carbon backing. This elastic scattering data was used for the solid angle normalization of the fission and monitor detectors, which is crucial for extracting the angular distributions of the binary fragments and the total fission cross sections.

A coincidence trigger between the front and back detectors was used for the ^{40}Ca+^{182}W, ^{192}Os reactions, while a singles trigger from the back detector was used for the elastic run. The monitor signals were also counted using scalers which were used for the monitor dead-time corrections. A pulser signal fed through the scaler and the data acquisition was used for dead-time correction in the fission data.

III. DATA ANALYSIS AND RESULTS

The delay line signals from each end of the position wire planes of the detectors were converted first into X and Y Cartesian coordinates in the detector reference frame. The detector coordinates were then transformed to spherical polar coordinates (θ and ϕ) using the information on the detector positions relative to the target. The calibrated position information, together with the time of flight information, was used to obtain the fragment velocities and center-of-mass angles assuming two-body kinematics [11,21–23]. This method allows us to obtain the mass ratio (M_R) of the fragments. Energy loss corrections were applied for the beam as well as for the fission fragments produced in the reaction, assuming that the interactions occurred at the center of the target. The fragment M_R distribution is then obtained by

$$M_R = \frac{m_1}{m_1 + m_2} = \frac{v_2}{v_1 + v_2}, \quad (1)$$

where m_1 and m_2 are the fragment masses at scission and v_1 and v_2 are the velocities of the fragments (in the center-of-mass frame) detected in the back and front detectors, respectively [22].

A. Mass-angle distributions

The mass-angle distributions (MADs) of the fragments from the ^{40}Ca+^{186}W and ^{40}C+^{192}Os reactions are shown in Figs. 1(a)–1(d) and in Figs. 2(a)–2(f), respectively. The E/V_B and CN excitation energy (E^*) values are given at the top of each plot, where E is the beam energy in center-of-mass and V_B is the capture barrier from a model [24] optimized for heavy systems.

MADs generally include all types of reaction products produced in the collision process with M_R values ranging from the entrance channel to mass symmetry. These products include groups from elastic, quasielastic, quasifission, and fusion-fission events. In reactions using fissile targets (ac-
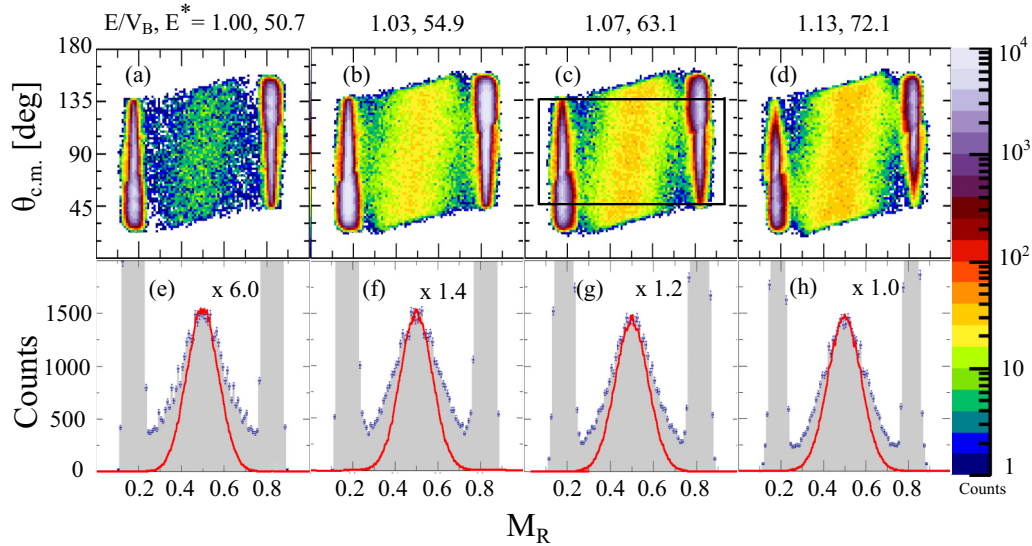
FIG. 1. Experimental MAD scatter plots for the ^{40}Ca+^{186}W reaction at different beam energies. The E/V_B values and CN excitation energies E* are given at the top of each plot. The corresponding projections of MADs [shown in panels (a)–(d)] onto the M_R axis are shown in the lower panels (e)–(h). These projections represent the experimental M_R distributions. The Gaussian distribution (red line) are the results of GEF calculations (see text).

tinides), in addition to these binary reaction products, there will also be a significant contribution from transfer-fission products in the experimental MADs [12,25]. This is not the case in the reactions studied here.

Since the fusion-fission products result from the decay of completely equilibrated CN, which retain no memory of how they were formed, the events are distributed in center-of-mass angle, often within a narrow band of M_R values between 0.4 and 0.6. For these events there is no correlation between mean mass and emission angle. Unlike fusion-fission, quasifission products result from a faster reseparation of the dinuclear system, well before reaching a fully shape equilibrated system. Hence, depending upon the sticking time (or time before

reseparation occurs), the products from this process may be seen with M_R values anywhere between the entrance channel M_R value and mass symmetry [1]. Reactions with very small sticking times result in mass-asymmetric quasifission. In this case, the system reseparates soon after capture (very small rotation angles) and the products are seen very close to the deep-inelastic events in terms of their M_R and angle values. The reactions with longer sticking times result in mass-symmetric quasifission and an overlap with fusion-fission events. The presence of quasifission could be inferred from the broader M_R widths [21,26,27] and larger angular anisotropies [23,28,29] than those expected for fusion-fission. Reactions with intermediate sticking times between these two extreme
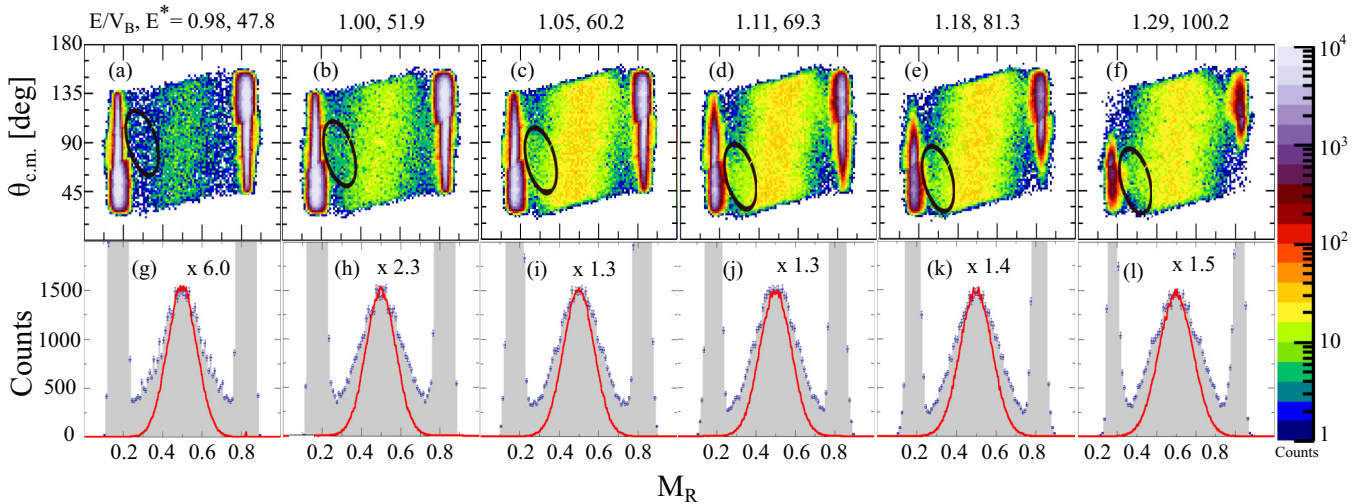

FIG. 2. Same as Fig. 1, but for the ^{40}Ca+^{192}Os reaction at different beam energies. The mass-asymmetric quasifission components present in the MADs are shown inside the black ellipses in panels (a)–(f). The Gaussian distributions (red line) are the results of GEF calculations (see text).

cases result in an anisotropic M_R distribution that shows a correlation between the mass and emission angle in the MADs. This correlation indicates that complete equilibration has not been achieved.

The MADs of both $^{40}Ca+^{182}W$ and $^{40}Ca+^{192}Os$ reactions show a significant correlation in the fragment mass and emission angle, indicating a strong contribution from quasifission. The features of the MADs do not show any significant change with increasing beam energy in both cases. A close inspection of the MADs indicates the presence of mass-asymmetric events between the quasielastic and the central band (which shows a mass-angle correlation) at all energies. These events are shown inside the ellipses (black color) in Figs. 2(a)–2(f). It may be noticed that the intensity of these events increases and their positions move toward forward angles with increasing beam energy. These are believed to be a mass-asymmetric quasifission component predominantly originating from the higher angular momentum collisions in the reaction, as discussed later.

B. M_R distributions

The M_R distributions of the fragments from the two reactions $^{40}Ca+^{186}W$ and $^{40}Ca+^{192}Os$ are shown in Figs. 1(e)–1(h) and in Figs. 2(g)–2(l), respectively. An angular window $(\Delta\theta)$ of width $90°$ has been selected for both the reactions [$45° < \Delta\theta < 135°$ as indicated by the rectangular box in Fig. 1(c)] before projecting the MADs onto M_R axis. This is to avoid biasing results due to the geometric limitations of the experimental setup. The counts at different E/V_B are scaled and the scaling factors are shown in each M_R plot.

By construction, the M_R distributions are peaked at mass symmetry for both reactions studied, at all energies. Within the experimental statistics, the distributions are consistent with a Gaussian form. The M_R distributions were thus fitted with a Gaussian function and the width of the M_R distribution is quantified by the standard deviation (σ_{MR}). These σ_{MR} values have contributions from fusion-fission and quasifission events. They are plotted against E/V_B in Fig. 3(a). The CN populated, CN excitation energy (E^*), and the σ_{MR} values at each E^* for the two reactions studied are given in Table I. The larger values of σ_{MR} at near-barrier energies suggest a stronger quasifission contribution and could be qualitatively explained by the deformation alignment [7,11] of the deformed targets used in this study. The value of σ_{MR} increases with beam energy above $E/V_B \sim 1.1$.

C. Minimum quasifission probability

The fission fragments produced from the fusion-fission process are peaked at mass symmetry and are expected to be distributed in a narrow range of M_R values, typically between 0.4 and 0.6. The width of this fusion-fission mass distribution may be calculated theoretically using the saddle-point [30,31] or the scission-point [32,33] models. This calculated σ_{MR} for the fusion-fission process and the experimental σ_{MR} obtained from the Gaussian fit can be used to estimate the minimum probability for the quasifission process in a given reaction [34]. However, since it is possible that the experimental σ_{MR}
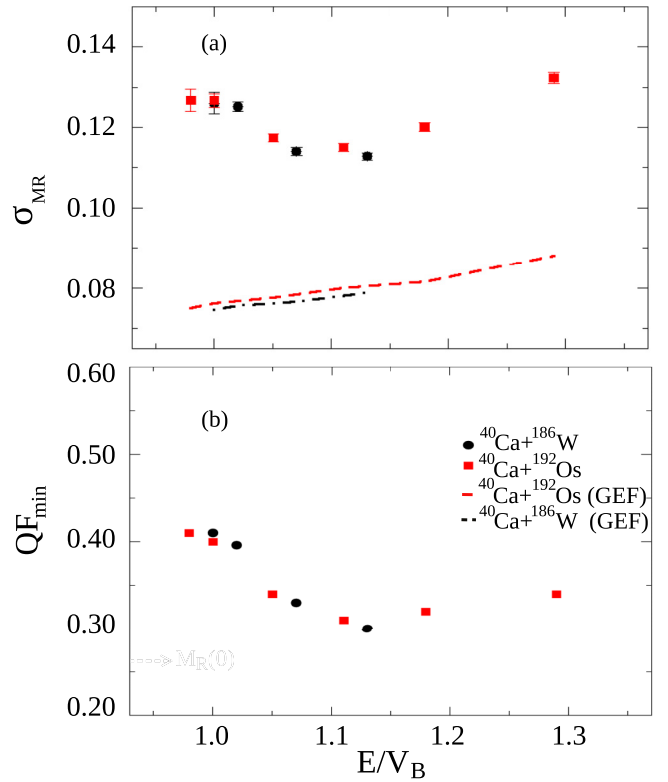

FIG. 3. (a) The solid points represent the experimental σ_{MR} values and the lines represent the σ_{MR} values calculated using GEF model. (b) The minimum quasifission probability as a function of E/V_B for the two reactions studied.

can have contributions from mass-symmetric quasifission, the estimated quasifission probability represents its lower limit (QF_{min}) at a given energy. The quantity $(1 - QF_{min})$ hence represents the maximum probability for CN formation for that reaction at that energy.

The variance of the fragment mass distribution from CN fission depends strongly on the temperature of the fissioning system. As the decision configuration is different in the saddle- and scission-point models, the calculation of nuclear temperature and hence the σ_{MR} values are very model sensitive.

TABLE I. Single Gaussian width obtained from fitting the M_R distributions for different systems studied in this work.

Reaction	CN	E^* (MeV)	σ_{MR}
$^{40}Ca+^{186}W$	^{226}Po	50.7	0.1260±0.0027
		54.9	0.1252±0.0012
		63.1	0.1141±0.0009
		72.1	0.1126±0.0008
$^{40}Ca+^{192}Os$	^{232}Cm	47.8	0.1268±0.0028
		51.9	0.1267±0.0017
		60.2	0.1174±0.001
		69.3	0.1150±0.0009
		81.3	0.1201±0.001
		100.2	0.1323±0.0014

This model dependency is less significant in lighter fissioning systems where saddle and scission points are not far apart [35,36], which is not the case for the reactions studied in this work. Hence, we used a semi-empirical GEneral description of Fission observables (GEF) model [37] to calculate σ_{MR} for the CN fission. GEF uses a large body of experimental information to develop an empirical, global description of fission quantities. The calculations have been performed by providing the excitation energy above the fission barrier (E_B^*), which is calculated as $E_B^* = E + Q - B_f(l) - E_{\rm rot} - E_{\rm pre}$, where $B_f(l)$ and $E_{\rm rot}$ are the angular-momentum-dependent fission barrier and rotation energy, calculated using the rotating finite-range model (RFRM) [38]. The average angular momentum values were obtained using coupled-channels calculations [39] by fitting the total capture cross sections calculated from the fragment angular distributions. Fragment angular distribution and total cross-section calculations are discussed in detail in Sec. III D. The energy carried away by the presaddle neutron emission is denoted by $E_{\rm pre}$. The presaddle neutron multiplicity is assumed to be half of the prescission neutron multiplicity ($N_{\rm pre}^{\rm sci}$) in this work. Hence $E_{\rm pre} = N_{\rm pre}^{\rm sci}/2 \times 10$ MeV, where the $N_{\rm pre}^{\rm sci}$ values are calculated following Ref. [31].

The calculated M_R distributions using the GEF model for the ^{40}Ca+^{186}W and ^{40}Ca+^{192}Os reactions at different E/V_B values are shown (solid red curves) along with the experimental M_R distributions in Figs. 1(e)–1(h) and in Figs. 2(g)–2(l), respectively. The σ_{MR} obtained from the Gaussian fits were used to calculate the QF$_{\rm min}$ and are plotted against E/V_B in Fig. 3(b). The dashed (red) and dot-dashed (black) lines in Fig. 3(a) correspond to the σ_{MR} values predicted by the GEF code for the ^{40}Ca+^{192}Os and ^{40}Ca+^{186}W reactions, respectively. The quantity QF$_{\rm min}$ ranges between 30 and 40% in the energy range of the present study, translating to a maximum compound nucleus formation probability of $\sim$60−70% in these reactions. It is likely that the true value is significantly smaller as analysis of the MADs shows in Sec. IV D.

D. Fragment angular distributions and capture cross sections

The large solid angle acceptance of the CUBE detectors provides an efficient way to collect the data with good statistics over a wide angular range in a single run. This was used to extract the angular distributions of the fragments and total fission cross sections for the two reactions in question. The data collected in the back detector were divided into angular bins each of width $\Delta\theta = 5°$ with a constant angular cut in ϕ. The yields of the binary fragments from each of these bins were used for calculating the differential cross sections, using the elastic yields recorded in the monitor detectors.

If Y_F and Y_M represent the yields in the fission and monitor detectors,

$$Y_F(\theta_{\rm lab}, E_{\rm lab}) = \left[\frac{d\sigma_F(\theta_{\rm lab}, E_{\rm lab})}{d\Omega_F}\right] \times d\Omega_F \times N_b \times N_t \tag{2}$$

and

$$Y_M(\theta_M, E_{\rm lab}) = \left[\frac{d\sigma_{\rm Ruth}(\theta_M, E_{\rm lab})}{d\Omega_M}\right] \times d\Omega_M \times N_b \times N_t, \tag{3}$$

where $\theta_{\rm lab}$ and θ_M are the mean angle of the fission bins (for example $\theta_{\rm lab} = 92.5°$ for the angular range of $90-95°$) and the monitor detector angle ($\theta_M = 23°$ in the present case), respectively. $d\Omega_F$ and $d\Omega_M$ represent the solid angle of the fission and monitor detectors, respectively. $E_{\rm lab}$ is the beam energy in the laboratory frame after correcting the energy loss in the target. N_b and N_t represent the numbers of beam and target nuclei available for the reaction.

From Eqs. (2) and (3),

$$\frac{Y_F(\theta_{\rm lab}, E_{\rm lab})}{Y_M(\theta_M, E_{\rm lab})} = \frac{d\Omega_F}{d\Omega_M} \frac{d\sigma_F(\theta_{\rm lab}, E_{\rm lab})/d\Omega_F}{d\sigma_{\rm Ruth}(\theta_M, E_{\rm lab})/d\Omega_M}, \tag{4}$$

$$\frac{d\sigma_F}{d\Omega_F} = \frac{Y_F}{Y_M} \frac{d\Omega_M}{d\Omega_F} \frac{d\sigma_{\rm Ruth}}{d\Omega_M}. \tag{5}$$

The solid angle normalization for individual bins in the fission detector (back) was performed using elastic scattering data. The ^{50}Cr+^{184}W reaction at 185.3 MeV beam energy was used as the calibration run for this experiment and the data collected in singles. The normalization was done in the laboratory frame. The dead-time corrections of the monitor and fission detector yields, efficiency loss due to the supporting wires, and the effects of beam pulsing system were taken into account in the analysis to calculate the fission differential cross sections.

The angular distributions of the binary fragments ($0.25 < M_R < 0.75$) from the two reactions at different beam energies are shown in Fig. 4 as a function of the center-of-mass angle. The total cross section is obtained by integrating the differential cross sections over the entire angular range. For this, an extrapolation of the distribution to the regions uncovered by the detector is necessary, which is done by fitting the distribution using the transition state model as described in Refs. [28,29]. These fits are represented by the dashed lines in Figs. 4(a) and 4(b).

The transition-state model calculations used here to fit the measured differential cross sections and extrapolate beyond the experimental acceptance of the detector assumes that the final direction of the binary fragments is given by the orientation of the nuclear symmetry axis when the compound system passes the saddle point. Also, the Coriolis force is assumed to be of insufficient strength to change the K value during the transition of the fissioning nucleus from the saddle point to scission point, where K is the projection of the total spin onto the nuclear symmetry axis. These conditions may not be satisfied if quasifission is present in a reaction. The experimental angular distribution thus deviates from the TSM predictions in such cases and yields larger angular anisotropies [23,29] over the TSM predictions. A signature of an obvious deviation may be noticed in the angular distribution at backward angles for the ^{40}Ca+^{186}W and ^{40}Ca+^{192}Os reactions in Fig. 4 at higher energies, further confirming the nonequilibrium nature of the reaction outcomes.
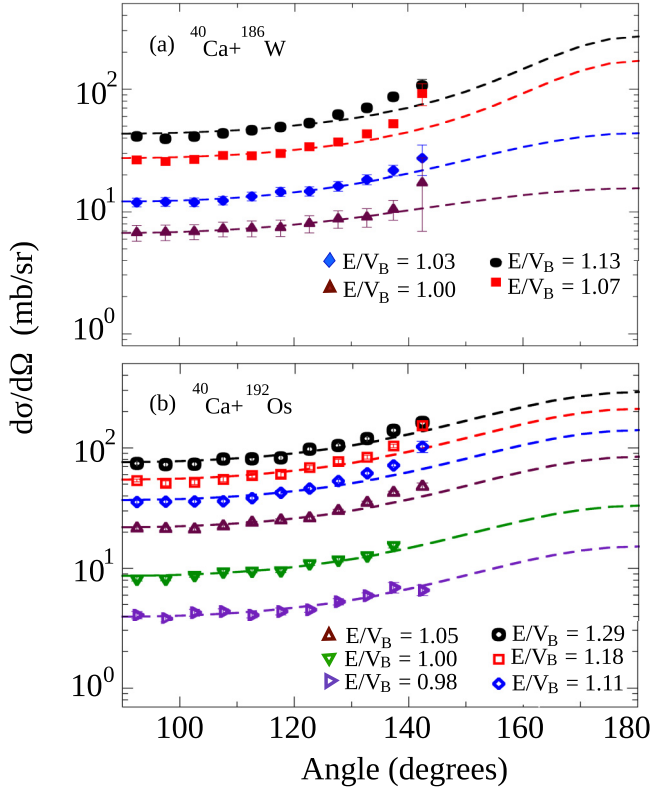
FIG. 4. The angular distributions (center-of-mass) of the binary fragments from the (a) ^{40}Ca+^{186}W and (b) ^{40}Ca+^{192}Os reactions at different beam energies. The broken lines are the fits obtained using the TSM (see text).

FIG. 5. Total fission cross sections for the ^{40}Ca+^{186}W and ^{40}Ca+^{192}Os reactions at different center-of-mass energies. The uncertainties are smaller than the symbols used.

Since we lack the differential cross section data at the extreme backward angles where the angular distribution deviates from $1/\sin\theta$ behavior, we do not attempt to quantify the angular anisotropies in this work. However, the integrated cross section is less sensitive to the angular anisotropies and does not vary significantly (less than 10%) with the fits assuming reasonable values of angular anisotropies. The total integrated cross sections thus obtained for the two reactions are shown in Fig. 5. These cross sections may be treated as the total capture cross sections, as the evaporation residue cross sections are expected to be negligibly small for these reactions.

IV. QUASIFISSION TIME SCALES

Now that we have the experimental MADs, angular distributions, and total capture cross sections for the two reactions studied in this work, we next attempt to estimate the time scales of the fast quasifission events present in these reactions by simulating the MADs, following a phenomenological approach [22,25]. This phenomenological model assumes classical trajectories for the incoming and outgoing particles. The angular displacements of the reaction products are related to the sticking time through calculated angular momentum distributions and moment of inertia. The details of the model can be obtained from Refs. [22,25].
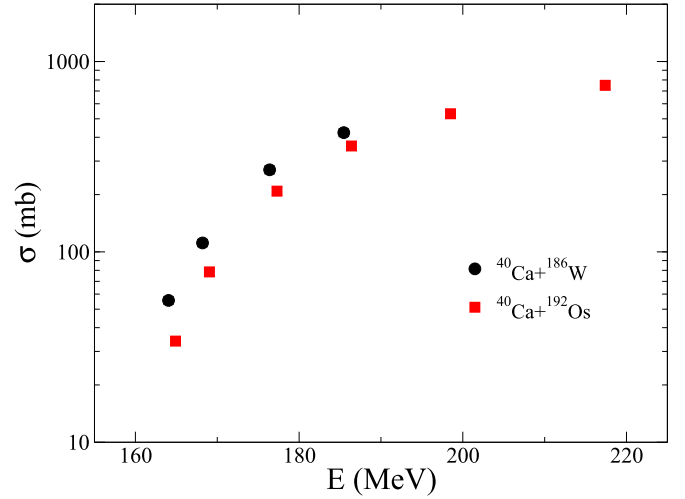
A. Angular momentum distributions—coupled-channels calculations

The capture angular momentum (ℓ) distributions were generated using the coupled-channels code CCMOD [39], which is a modified version of CCDEF [40]. It is assumed that collisions up to a critical angle ($25°$ [25]) between the projectile direction and target deformation axis were assumed as axial collisions. These axial collisions offer lower barriers to capture in the case of reactions using prolately deformed targets and are shown to result predominantly in fast quasifission events [7,11]. All other collisions were treated as equatorial collisions, which offer higher barriers to capture and are assumed to end up in fusion-fission or slow quasifission events. For each beam energy, ℓ distributions were generated separately for the axial and equatorial events and the simulations were separately performed for these events using different sticking time distributions [25].

1. Selection of bare potential

In coupled-channels calculations, an energy-independent Woods-Saxon potential of the following form is generally used:

$$V_N(r) = \frac{-V_0}{1 + \exp\left[(r - r_0 \times (A_P^{\frac{1}{3}} + A_T^{\frac{1}{3}}))/a\right]} \quad (6)$$

where V_0 is the depth of the potential in MeV, a is the diffuseness parameter, and r_0 is the radius parameter [41,42]. A_P and A_T are the masses of the projectile and target nuclei, respectively. The choice of the potential parameters is very important and should be done with utmost care in coupled-channels calculations as these parameters have a strong influence on the calculation results. It is reported that larger values of a ranging between 0.75 and 1.5 fm [43] were required to reproduce the fusion-capture cross sections at above-barrier energies compared with the $a \sim 0.65$ fm [44–46] obtained from the analysis of sub-barrier elastic
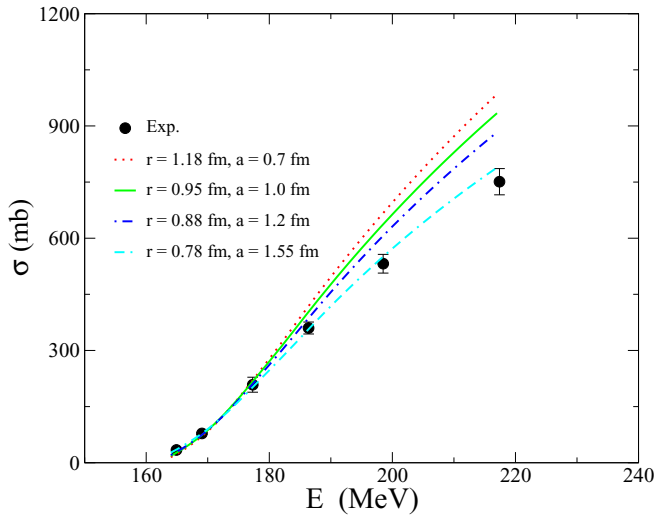
FIG. 6. Coupled-channels calculations for the ^{40}Ca+^{192}Os reactions with different potential parameters.

scattering data. The effect of different diffuseness parameters in reproducing the total capture cross sections is explored in detail for the reactions studied and is discussed below.

In this work, the potential parameters were selected in the following manner: V_0 is chosen to be sufficiently deep to contain all partial waves. The values of a and r_0 were adjusted until the Swiatecki [24] capture barrier is reproduced without coupling any of the internal degrees of freedom. The couplings were then added to include the static deformation of the target and the parameters were once again adjusted to match the Swiatecki capture barrier [24]. In both reactions, ^{40}Ca+^{186}W and ^{40}Ca+^{192}Os, it is observed that the potential parameters assuming $a \sim 0.7$ fm overpredict the capture cross sections, particularly at higher energies. Predictions for different diffuseness parameters for the ^{40}Ca+^{192}Os reaction are shown in Fig. 6, for example, consistent with earlier studies of fusion of heavy nuclei [43]. It is clear that a large value of diffuseness parameter ~ 1.5 fm is required to fit the cross sections, possibly indicating fusion hindrance at higher energies due to dissipative effects or a failure of the coupled-channels code to deal with dynamical aspects of fusion. The final values of the potential parameters used in the coupled-channels calculations are shown in Table II.

2. Coupling of nuclear structure effects

The nuclear structure effects play a significant role in fusion cross section and ℓ distributions, particularly at the near- and

TABLE II. The Swiatecki model capture barrier (V_B in MeV) in center-of-mass frame and the Woods-Saxon potential parameters (V_0, a and r_0) used to reproduce capture cross sections for the reactions studied in this work.

Reaction	CN	V_B (MeV)	V_0(MeV)	a (fm)	r_0 (fm)
^{40}Ca+^{186}W	^{226}Po	164.5	381	1.3	0.85
^{40}Ca+^{192}Os	^{232}Cm	168.2	393	1.55	0.78

sub-barrier energies. At above-barrier energies, the calculated ℓ distribution is not very different with or without couplings as long as the capture cross sections are reproduced [47,48]. As we do not have experimental barrier distribution available for the reactions studied in this work, a rigorous calculation has not been attempted for the reactions reported. Also, the gross features in the MADs are less sensitive to such effects. The static deformation of the target nucleus and the inelastic couplings of the projectile-target nucleus were included in the present calculations for reproducing the cross sections and generating the ℓ distributions for the axial and equatorial events. The effect of deformation alignment of the target used in the reaction is found to be more significant at near-barrier energies and decreases with increasing beam energy. This effect is expected to reflect the varying relative yields of axial and equatorial collisions with beam energy [11]. Care was taken in the MAD simulations to make sure that the relative yield of the axial and equatorial collisions show this expected trend with beam energy.

The effect of deformation is more important than other (vibrational) couplings, as it produces a wide range of barriers which dictate the orientations that lead to the capture at a given energy. The details of other couplings are not so important for extracting the ℓ distribution, as long as the capture cross sections are reproduced. However, for the sake of completeness, details of all the couplings used in the calculations are described in the appendix.

In reactions using prolate deformed targets, axial collisions offer lower barriers to capture due to larger radial separation. This is observed to be true for the ^{40}Ca+^{186}W reaction. Hence, collisions up to $25°$ between the projectile direction and target deformation angle were treated as axial collisions for the ^{40}Ca+^{186}W reaction and the ℓ distributions were generated accordingly. Such collisions are likely to end up in a fast quasifission process [11,12,49] at near-barrier energies. However, it is observed that the same definition does not hold for the ^{40}Ca+^{192}Os reaction. The Coloumb barriers for the two reactions at different orientation angles of the ^{186}W and ^{192}Os target nuclei relative to the beam direction are shown in Fig. 7. Though the lowest barriers for capture are associated with the lower angle collisions in the case of ^{40}Ca+^{186}W reaction as seen in Fig. 7(a), the scenario is different for the ^{40}Ca+^{192}Os reaction as shown in Fig. 7(b), where the lowest barriers to capture are not associated with the lower angle collisions. This is due to the comparatively small β_2 and large β_4 values of the ^{192}Os nucleus compared with that of ^{186}W or of actinide nuclei. Hence the ℓ distributions generated for the events with collision angles between $25°$ and $50°$ were used for simulating the fast quasifision events in the case of the ^{40}Ca+^{192}Os reaction. As a result, instead of the terms axial and equatorial collisions used so far, we use the terms "lower barrier collisions" for the collisions leading to fast quasifission and "higher barrier collisions" for all other collisions.

B. Moment of inertia

In a previous work on the ^{34}S+^{232}Th reaction [25], we used the average moment of inertia calculated using the time-dependent Hartree-Fock (TDHF) theory for simulating
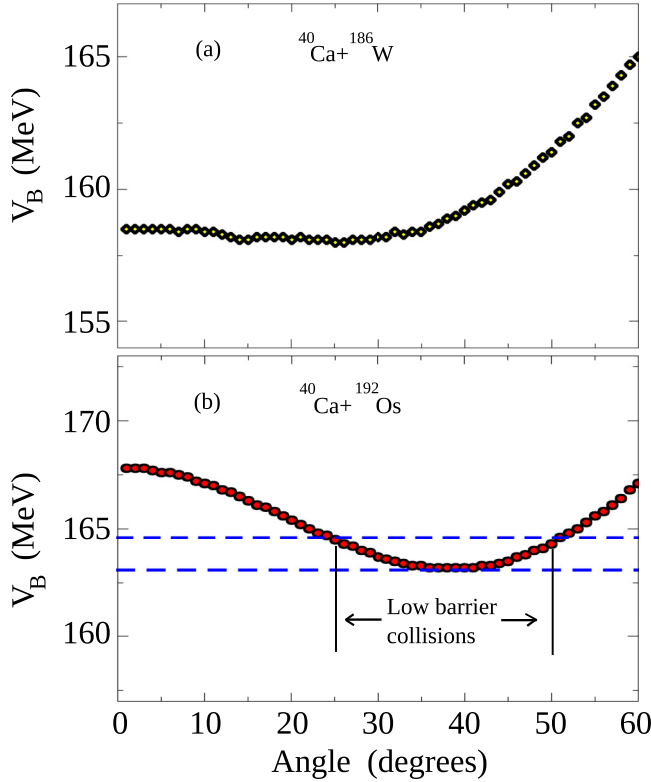
FIG. 7. The Coulomb barrier as a function of different orientation angles of the (a) ^{186}W and (b) ^{192}Os nuclei relative to the beam direction, for the reactions studied.

the MADs. In the absence of TDHF calculations for these reactions, the average values of the moment of inertia used for the current systems were obtained from that of the ^{34}S+^{232}Th reaction using a scaling procedure. The scaling factor is determined from the ratio of the TDHF moment of inertia and the rigid body moment of inertia calculated for the ^{34}S+^{232}Th reaction with projectile and target at touching configuration. The projectile is assumed to be a sphere and the target is treated as a prolate spheroid in this calculation.

C. Mass drift and sticking-time distributions

We used the exponential form of the mass drift function [1] to describe the mass evolution after contact. In this expression, the mass evolves asymptotically toward mass symmetry. The average M_R after a sticking time t_s is given by

$$M_R(t) = [M_R(0) - 0.5]e^{-t_s/\tau_m} + 0.5, \quad (7)$$

where the initial mass ratio is given by $M_R(0) = A_T/(A_T + A_P)$. The parameter τ_m denotes the mass equilibration time constant. The above mass drift function describes an asymptotic mass drift to $M_R = 0.5$ with a rapid mass flow in the early stages of contact. The simulations have been performed separately for the lower barrier and higher barrier collisions with $\tau_m = 5.2$ zs in the beginning, where 1 zs $= 10^{-21}$ s.

As described in Ref. [25], the M_R values were calculated using a randomly chosen sticking time t_s, which follows a distribution assumed to be a half-Gaussian function followed by

an exponential fall. Such a distribution is characterized by the Gaussian peak (p), standard deviation (s), and the exponential fall time (e). As collisions with different orientations of the deformed target result in different reaction outcomes based on their sticking times, different sticking-time distributions were used for the lower barrier and higher barrier collisions. It was previously demonstrated that lower barrier collisions predominantly lead to fast quasifission [7,11,49–51] as the elongation is far outside the saddle point and the system reseparates soon after contact, while higher barrier collisions, which result in more compact contact configurations, stay together for a longer duration and evolve toward a more mass-equilibrated configuration. Hence, a shorter t_s distribution was used for the collisions leading to fast quasifission. The parameters (p, s, and e) were varied to reproduce M_R and angular distributions, simultaneously. The mass-symmetric component, which is assumed to originate from the higher barrier collisions, are simulated using a long t_s distribution with the same parameters $(p,s,e) = (24,8,20)$ zs as used in our previous work [25]. Such a long t_s distribution allows the dinuclear system to remain intact for a longer duration and hence achieve essentially complete mass equilibration.

D. MAD simulations

Using the basic ingredients discussed in the previous sections, first we attempted to reproduce the experimental MADs using the simulation described above with the exponential mass evolution function described by Eq. (7). The discussion below of sticking times and mass evolution applies to the lower barrier collisions (tip collisions for the ^{40}Ca+^{186}W reaction), which are dominant at lower beam energies.

1. ^{40}Ca+^{186}W *reaction*

The experimental and simulated MAD at the lowest energy measured ($E/V_B = 0.98$) are shown in Figs. 8(a) and 8(c), respectively. The simulations have been performed for a larger angular range (10° to 170° in the center-of-mass) excluding quasielastic events. The M_R distribution is obtained by projecting the MADs on to the M_R axis. Only the events with $\theta_{c.m.}$ between 45° and 135° and M_R values between 0.25 and 0.75 were used to generate the M_R distribution and are shown in Fig. 8(b). While the angular limits are imposed to avoid the effect of the geometrical acceptance of the detectors used, limits on M_R values were used to exclude the quasielastic events. The experimental angular distribution for the lighter fragments ($0.25 < M_R < 0.5$) is shown in Fig. 8(d).

The t_s parameters (p, s, and e) required for reproducing the major quasifission component in the reactions studied at different E/V_B values and the average sticking times are shown in Table III. Even though simulations using the standard [1] mass-drift function and mass equilibration time constant ($\tau_m = 5.2$ zs) can reproduce the gross features of the experimental MAD reasonably well, slight disagreements may be observed in the M_R distributions at larger mass asymmetries and angles in the region roughly between 60° and 90° in center-of-mass, as shown by the broken (black) rectangles in Figs. 8(b) and 8(d). A similar observation was also made for the ^{40}Ca+^{192}Os reaction. A close inspection
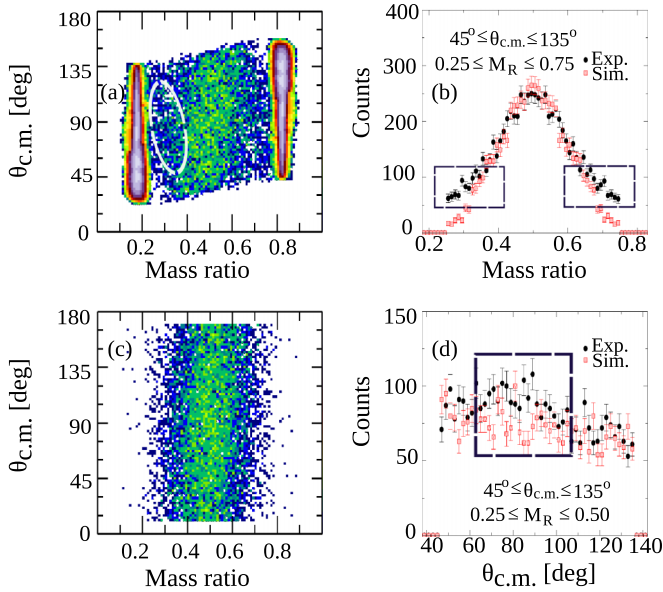
FIG. 8. (a) Experimental and (c) simulated MAD for the ^{40}Ca+^{186}W reaction at $E/V_B = 0.98$. Simulations are performed assuming the standard mass-drift function and mass-equilibration time constant [1]. Quasielastic events are excluded in the MAD simulations shown in panel (c). (b) Experimental and simulated M_R distributions for the ^{40}Ca+^{186}W reaction at same beam energy. (d) Experimental (black circle) and simulated (red square) angular distributions of the fragments with M_R values between 0.25 and 0.5. The color scale for the counts in the MADs are the same as Fig. 1.
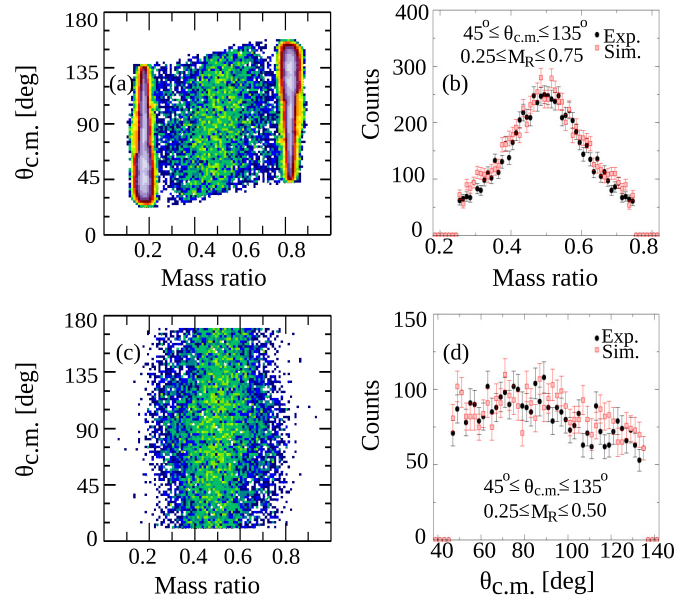

FIG. 9. The (a) experimental and (c) simulated MAD including the mass-asymmetric component for the ^{40}Ca+^{186}W reaction at $E/V_B = 0.98$. This mass-asymmetric component is generated from the lower barrier ℓ distribution with $\ell > 40\hbar$. (b) Experimental and simulated M_R distributions. (d) Experimental (black circle) and simulated (red square) angular distributions of the fragments with M_R values betweem 0.25 and 0.5. The color scales for the counts in the MADs are the same as in Fig. 1.

of the experimental MAD shown in Fig. 8(a) indicates the presence of a mass-asymmetric component that appears to have evolved less in mass compared with other events between the quasielastic band and the strongly correlated central band, as shown inside the ellipse (broken, white color). These events are absent in the simulated MAD shown in Fig. 8(c) assuming an exponential mass evolution [Eq. (7)] with a constant $\tau_m = 5.2$ zs. This component possibly causes the observed differences in the M_R and angular distributions highlighted by the rectangles in Figs. 8(b) and 8(d).

To simulate these events, the ℓ distributions for the lower barrier collisions were calculated. The higher angular

TABLE III. The parameters of the sticking-time distribution and average sticking time for the quasifission components (which show a strong mass-angle correlation) at different beam energies The slow quasifission and fusion-fission events are simulated with a longer sticking-time distribution (see text).

Reaction	E/V_B	p,s,e (zs)	Average t_s (zs)
	0.98	10.7, 2.0, 1.6	10.3
	1.03	9.6, 2.2, 2.5	9.9
^{40}Ca+^{186}W	1.07	10.0, 2.8, 2.6	9.8
	1.13	9.2, 2.8, 3.0	9.3
	1.0	10.4, 2.0,2.2	10.5
^{40}Ca+^{192}Os	1.05	9.6, 2.0,1.8	9.4
	1.11	9.5, 2.0,1.6	9.2

momentum ($\ell > 40\hbar$) collisions were given shorter average sticking times and a τ_m value different from 5.2 zs, and the case is investigated. Such a scenario with beam-energy-dependent τ_m was previously reported in the case of ^{34}S+^{23}Th reaction forming ^{266}Sg [25]. Simulations using a t_s distribution with average sticking time of 10.3 zs and $\tau_m = 5.2$ zs for the lower barrier collisions reproduce the major quasifission band in the MAD. The higher angular momentum, mass-asymmetric events required an average sticking time of ~ 6 zs and $\tau_m \sim 14$ zs at $E/V_B = 0.98$. The resulting M_R and $\theta_{c.m.}$ distributions at $E/V_B = 0.98$ are compared with experiment in Figs. 9(b) and 9(d).

Though weaker in intensity compared with the events that show a mass-angle correlation in the central band, the mass-asymmetric quasifission component is also present at higher bombarding energies. Such events in the ^{40}Ca+^{186}W reaction are shown inside the black ellipses in Figs. 10(a)–10(c), for example. As demonstrated in the case of $E/V_B = 0.98$, these events can be generated from the higher angular momentum collisions—shown in the simulations in Figs. 10(c)–10(e)—with an average sticking time of 5–6 zs and mass equilibration constant between 14 and 18 zs. An interesting observation is the average sticking time of the quasifission events which show mass-angle correlations in the experimental MAD plots. Sticking time distributions with average sticking time of 9–10 zs is required to simulate these correlated events in the experimental MADs, in the entire range of energies studied in this work. The simulation results are compared with experimental results for different E/V_B values in Fig. 10.
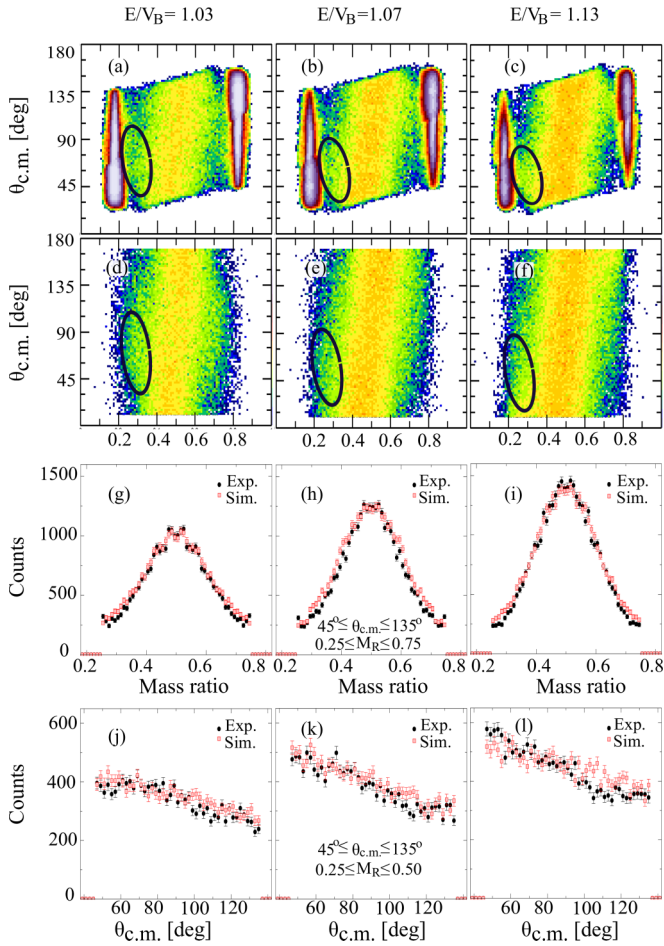
FIG. 10. Plots (a)–(c): Experimental MADs for the ^{40}Ca+^{186}W reaction at different beam energies. Plots (d)–(f): Corresponding simulated MADs for the same reaction. Plots (g)–(i): Experimental (black circles) and simulated (red squares) M_R distributions. The same gating conditions used in Fig. 8(d) are followed to generate the M_R distributions. Plots (j)–(l): Experimental (black circles) and simulated (red squares) angular distributions of the fragments with M_R values between 0.25 and 0.5 with the same gating conditions as in Fig. 8(c). The weak mass asymmetric quasifission component present in the reaction are indicated inside the ellipse (black) in the experimental and simulated MADs. The color scale for the counts in the MADs are the same as Fig. 1.

The experimental MADs are shown in Figs. 10(a)–10(c) and the simulation results are shown in Figs. 10(d)–10(f). The experimental and simulated M_R distributions of the fragments with $0.25 < M_R < 0.75$ are shown in Figs. 10(g)–10(f) and angular distributions of the light fragments ($0.25 < M_R < 0.5$) are shown in Figs. 10(j)–10(l). Very good agreement has been observed in the experimental and simulated M_R and angular distributions in the entire range of M_R values and angles considered, at all E/V_B values.

2. ^{40}Ca+^{192}Os *reaction*

MAD simulations have also been performed for the ^{40}Ca+^{192}Os reaction at three beam energies ($E/V_B = 1.0$, 1.05 and 1.11). An average sticking time of $\sim 9-11$ zs
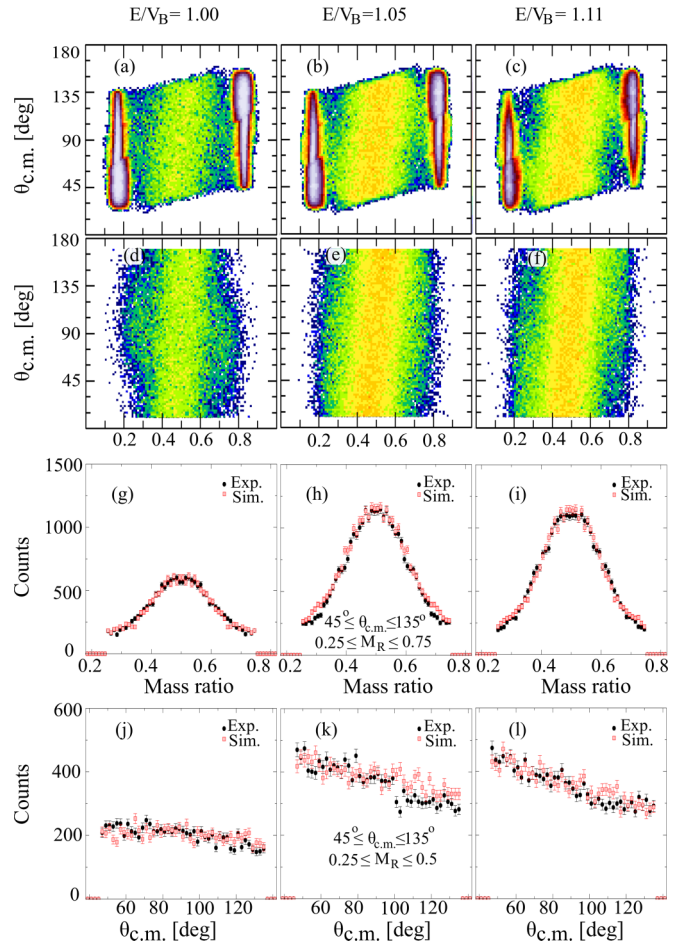
FIG. 11. Same as Fig. 10, but for the ^{40}Ca+^{192}Os reaction at different beam energies.

is required to reproduce the experimental MADs in the energy range that was chosen for the simulations. As in the case of the ^{40}Ca+^{186}W reaction, the simulations for all bombarding energies use a shorter sticking time for the high angular momentum ($\ell > 40\hbar$) collisions with the lower energy barriers. The results of the simulation are compared with experimental results for different E/V_B values in Fig. 11.

V. DISCUSSION AND CONCLUSION

In this paper, we report the fission fragment mass ratio and angular distribution measurements and phenomenological simulations to calculate the quasifission time scales for the ^{40}Ca+^{186}W and ^{40}Ca+^{192}Os reactions. MADs of both reactions show a strong mass-angle correlation, indicating the presence of quasifission. The width of the M_R distribution shows an increasing trend with decreasing energy at near-barrier energies, which is a clear indication of the effect of deformation alignment of the targets used in the study.

The minimum quasifission probability is calculated from the ratio of the experimental σ_{MR} and the σ_{MR} expected for the fusion-fission events calculated using the semiempirical model GEF. It has been observed that the minimum quasifission probability ranges between 30% and 40% in the energy range

of the present work. This means that the maximum fusion probability is $60-70\%$ for these reactions in the energy range of present study. Existing parametrizations [52,53] predict P_{CN} values an order of magnitude less than the maximum value obtained in this work. From fission fragment angular distribution measurements, Yanez *et al.* [54] also concluded that the current models [52,53] are not adequate for quantitatively specifying the P_{CN} values in heavy-ion fusion reactions. However, it should also be mentioned that the deduced P_{CN} values for the ^{30}Si+^{197}Au and ^{36}S+^{197}Au reactions [54] are much lower than the maximum values obtained for the more mass-symmetric reactions studied in this work. Hence, the experimental determination of P_{CN} values for various reactions using heavy projectiles is important to establish a more reliable parametrization for P_{CN} and thereby model fusion in heavy systems.

The total fission cross sections are determined from the fragment angular distributions. These cross sections represent the total capture cross sections as the evaporation residue cross sections are expected to be negligibly small in these reactions. Since we lack differential cross section data at the extreme backward angles, we did not attempt to quantify the angular anisotropies in this work.

It is interesting to observe that the coupled-channels calculations, assuming the standard Woods-Saxon parametrization of the nuclear potential with a diffuseness parameter $a = 0.65$ fm, overpredict the capture cross sections for both reactions. It is well known that $a \sim 0.65$ fm is required to reproduce the elastic and quasielastic data [44–46]. However, to reproduce the experimental cross sections, larger values of a, around 1.5 fm, are required for the reactions studied in this work. A systematic study by Newton *et al.* [43] previously reported an increasing trend of a with increase in charge product $(Z_P Z_T)$ by analyzing the fusion excitation function for a number of reactions using coupled-channels calculations, and the observed effect was attributed to the possibility of fusion inhibition originating from the energy dissipative processes at high excitations. It may be argued that the current observations in the case of ^{40}Ca+^{186}W and ^{40}Ca+^{192}Os reactions could be an indication of fusion inhibition in these reactions at higher energies. It may also be mentioned that such dynamical effects are not included in standard coupled-channels models. Hence, capture excitation functions for reactions with larger $Z_P Z_T$ should be helpful for understanding more about the dynamical aspects of fusion at higher excitation energies and thereby refining the existing coupled-channels models.

The MAD simulations using the phenomenological model reveal that quasifission components that show strong mass-angle correlations have average time scales of ~ 10 zs in the reactions studied. Similar sticking times were previously reported for the ^{48}Ti+^{186}W reaction [23,55], which also showed similar features in the experimental MADs. Longer sticking times were observed for the ^{40}Ca+^{186}W and ^{40}Ca+^{192}Os reactions compared with that of ^{34}S+^{232}Th reaction ($t_s \sim$ 7 zs [25]); this is consistent with the fact that more mass equilibration has been achieved in the former case in comparison with the latter one, as is evident from their respective MADs. However, the presence of a mass-angle correlation in the ^{40}Ca+^{186}W and ^{40}Ca+^{192}Os reactions confirms that the

dinuclear system should stay together for a longer duration than 10 zs to achieve complete equilibration in mass and shape degrees of freedom.

Finally, it should be mentioned that the small component of mass-asymmetric quasifission present in both reactions at all bombarding energies could be explained as resulting from the high-angular-momentum low-barrier collisions. Such collisions are associated with a shorter average sticking time compared with the quasifission component present in the central band in the MADs which show a mass-angle correlation. These events could not be reproduced by assuming an exponential mass-drift function with $\tau_m = 5.2$ zs. Instead, larger mass-equilibration constant (14–18 zs) is required to reproduce such events. Though this observation may be questioned with the limited statistics available and possible the uncertainities in the simulation originating from the inputs (angular momentum distribution and moment of inertia), such a situation was shown to successfully account for the mass-asymmetric quasifission component in the reaction forming ^{266}Sg [25]. The exponential mass drift function with $\tau_m = 5.2$ zs [1] predicts a very rapid mass drift toward mass symmetry after contact. The failure of such a parametrization to reproduce the mass-asymmetric component thus hints at the possibility that mass evolution is not as monotonic as described by the exponential function [1] with a constant mass equilibration time constant.

The average position of this mass-asymmetric group is seen to move toward forward angles with increasing beam energy, which indicates a relationship with the angular momentum of the heavy-ion collision. Successful reproduction of this mass-asymmetric component using the higher angular momentum and lower barrier ℓ distribution shows the potential of the simple, classical simulation to explore the effects of higher angular momentum collisions in heavy-ion reactions.

APPENDIX

For the ^{40}Ca+^{186}W reaction, the measured capture cross sections could be reasonably well represented by the calculation incorporating the static deformation of the target nucleus ($\beta_2 = 0.28$, $\beta_4 = -0.07$ [56]) and inelastic couplings to the 2^+ and 3^- states of ^{40}Ca and 3^- states of ^{186}W. For the reaction with the ^{192}Os target, $\beta_2 = 0.155$, $\beta_4 = -0.081$ [57], inelastic couplings to 2^+, 3^- states of ^{40}Ca and 3^- state of the ^{192}Os nuclei were used in the calculations. The inelastic coupling strengths were included using

$$F_{\text{inel}}(r) = \frac{\beta_\lambda}{\sqrt{4\pi}} \left[-R \frac{dV_n(r)}{dr} + \frac{3Z_1 Z_2 e^2}{(2\lambda + 1)} \frac{R^\lambda}{r^{\lambda+1}} \right], \quad \text{(A1)}$$

where β_λ is the deformation parameter associated with the multipolarity λ, R (taken to be 1.06 $A^{\frac{1}{3}}$ fm, following Ref. [56]) is the radius of the excited nucleus, and $V_n(r)$ is the nuclear potential. The deformation parameters for different λ were generally taken from the calculated or measured transition probabilities [57–59].

[1] J. Tōke, R. Bock, G. X. Dai, A. Gobbi, S. Gralla, K. D. Hildenbrand, J. Kuzminski, W. F. J. Müller, A. Olmi, H. Stelzer *et al.*, Nucl. Phys. A **440**, 327 (1985).

[2] W. J. Swiatecki, Phys. Scr. **24**, 113 (1981).

[3] J. P. Blocki, H. Feldmeier, and W. J. Swiatecki, Nucl. Phys. A **459**, 145 (1986).

[4] W. Q. Shen, J. Albinski, A. Gobbi, S. Gralla, K. D. Hildenbrand, N. Herrmann, J. Kuzminski, W. F. J. Muller, H. Stelzer, J. Toke *et al.*, Phys. Rev. C **36**, 115 (1987).

[5] K. Nishio, H. Ikezoe, S. Mitsuoka, I. Nishinaka, Y. Nagame, Y. Watanabe, T. Ohtsuki, K. Hirose, and S. Hofmann, Phys. Rev. C **77**, 064607 (2008).

[6] K. Nishio, S. Mitsuoka, I. Nishinaka, H. Makii, Y. Wakabayashi, H. Ikezoe, K. Hirose, T. Ohtuski, Y. Aritomo, and S. Hofmann, Phys. Rev. C **86**, 034608 (2012).

[7] D. J. Hinde, R. G. Thomas, R. du Rietz, A. Diaz-Torres, M. Dasgupta, M. L. Brown, M. Evers, L. R. Gasques, R. Rafiei, and M. D. Rodriguez, Phys. Rev. Lett. **100**, 202701 (2008).

[8] A. C. Berriman, D. J. Hinde, M. Dasgupta, C. R. Morton, R. D. Butt, and J. O. Newton, Nature (London) **413**, 144 (2001).

[9] C.-C. Sahm, H.-G. Clerc, K.-H. Schmidt, W. Reisdorf, P. Armbruster, F. P. Heßberger, J. G. Keller, G. Münzenberg, and D. Vermeulen, Z. Phys. A **319**, 113 (1984).

[10] D. J. Hinde and M. Dasgupta, Phys. Lett. B **622**, 23 (2005).

[11] D. J. Hinde, M. Dasgupta, J. R. Leigh, J. C. Mein, C. R. Morton, J. O. Newton, and H. Timmers, Phys. Rev. C **53**, 1290 (1996).

[12] D. J. Hinde, R. du Rietz, M. Dasgupta, R. G. Thomas, and L. R. Gasques, Phys. Rev. Lett. **101**, 092701 (2008).

[13] C. Simenel, D. J. Hinde, R. du Rietz, M. Dasgupta, M. Evers, C. J. Lin, D. H. Luong, and A. Wakhle, Phys. Lett. B **710**, 607 (2012).

[14] D. J. Hinde, M. Dasgupta, M. Evers, C. J. Lin, D. H. Luong, R. du Rietz, C. Simenel, A. Wakhle, and E. Williams, J. Phys.: Conf. Ser. **420**, 012115 (2013).

[15] S. Hofmann and G. Munzenberg, Rev. Mod. Phys. **72**, 733 (2000).

[16] S. Hofmann, Lect. Notes Phys. **764**, 203 (2009).

[17] Y. T. Oganessian, J. Phys. G: Nucl. Part. Phys. **34**, R165 (2007).

[18] Y. T. Oganessian, F. S. Abdullin, P. D. Bailey, D. E. Benker, M. E. Bennett, S. N. Dmitriev, J. G. Ezold, J. H. Hamilton, R. A. Henderson, M. G. Itkis *et al.*, Phys. Rev. Lett. **104**, 142502 (2010).

[19] Y. T. Oganessian and V. K. Utyonkov, Rep. Prog. Phys. **78**, 036301 (2015).

[20] E. Prasad, D. J. Hinde, K. Ramachandran, E. Williams, M. Dasgupta, I. P. Carter, K. J. Cook, D. Y. Jeung, D. H. Luong, S. McNeil *et al.*, Phys. Rev. C **91**, 064605 (2015).

[21] R. Rafiei, R. G. Thomas, D. J. Hinde, M. Dasgupta, C. R. Morton, L. R. Gasques, M. L. Brown, and M. D. Rodriguez, Phys. Rev. C **77**, 024606 (2008).

[22] R. du Rietz, E. Williams, D. J. Hinde, M. Dasgupta, M. Evers, C. J. Lin, D. H. Luong, C. Simenel, and A. Wakhle, Phys. Rev. C **88**, 054618 (2013).

[23] E. Williams, D. J. Hinde, M. Dasgupta, R. du Rietz, I. P. Carter, M. Evers, D. H. Luong, S. D. McNeil, D. C. Rafferty, K. Ramachandran, and A. Wakhle, Phys. Rev. C **88**, 034611 (2013).

[24] W. J. Świątecki, K. Siwek-Wilczyńska, and J. Wilczyński, Phys. Rev. C **71**, 014602 (2005).

[25] E. Prasad, A. Wakhle, D. J. Hinde, E. Williams, M. Dasgupta, M. Evers, D. H. Luong, G. Mohanto, C. Simenel, and K. Vo-Phuoc, Phys. Rev. C **93**, 024607 (2016).

[26] E. Prasad, K. M. Varier, R. G. Thomas, P. Sugathan, A. Jhingan, N. Madhavan, B. R. S. Babu, R. Sandal, S. Kalkal, S. Appannababu *et al.*, Phys. Rev. C **81**, 054608 (2010).

[27] A. Shamlath, M. Shareef, E. Prasad, P. Sugathan, R. G. Thomas, A. Jhingan, S. Appannababu, A. K. Nasirov, A. M. Vinodkumar, K. M. Varier *et al.*, Nucl. Phys. A **945**, 67 (2016).

[28] B. B. Back, R. R. Betts, K. Cassidy, B. G. Glagola, J. E. Gindler, L. E. Glendenin, and B. D. Wilkins, Phys. Rev. Lett. **50**, 818 (1983).

[29] B. B. Back, R. R. Betts, J. E. Gindler, B. D. Wilkins, S. Saini, M. B. Tsang, C. K. Gelbke, W. G. Lynch, M. A. McMahan, and P. A. Baisden, Phys. Rev. C **32**, 195 (1985).

[30] G. N. Knyazheva, E. M. Kozulin, R. N. Sagaidak, A. Y. Chizhov, M. G. Itkis, N. A. Kondratiev, V. M. Voskressensky, A. M. Stefanini, B. R. Behera, L. Corradi *et al.*, Phys. Rev. C **75**, 064602 (2007).

[31] M. G. Itkis and A. Ya. Rusanov, Phys. Part. Nucl. **29**, 160 (1998).

[32] P. D. Bond, Phys. Rev. Lett. **52**, 414 (1984).

[33] H. H. Rossner, J. R. Huizenga, and W. U. Schröder, Phys. Rev. Lett. **53**, 38 (1984).

[34] C. J. Lin, R. du Rietz, D. J. Hinde, M. Dasgupta, R. G. Thomas, M. L. Brown, M. Evers, L. R. Gasques, and M. D. Rodriguez, Phys. Rev. C **85**, 014611 (2012).

[35] M. G. Itkis, N. A. Kopndrat'ev, S. I. Mul'gin, V. N. Okolovich, A. Ya. Rusanov, and G. N. Smirenkin, Yad. Fiz. **52**, 944 (1990).

[36] M. G. Itkis, V. N. Okolovich, A. Ya. Rusanov, and G. N. Smirenkin, Z. Phys. A **320**, 433 (1985).

[37] K.-H. Schmidt, B. Jurado, C. Amouroux, and C. Schmitt, Nuclear Data Sheets **131**, 107 (2016).

[38] A. J. Sierk, Phys. Rev. C **33**, 2039 (1986).

[39] M. Dasgupta, A. Navin, Y. K. Agarwal, C. V. K. Baba, H. C. Jain, M. L. Jhingan, and A. Roy, Nucl. Phys. A **539**, 351 (1992).

[40] C. H. Dasso and S. Landowne, Comput. Phys. Commun. **46**, 187 (1987).

[41] C. Simenel, M. Dasgupta, D. J. Hinde, and E. Williams, Phys. Rev. C **88**, 064604 (2013).

[42] C. Simenel, A. S. Umar, K. Godbey, M. Dasgupta, and D. J. Hinde, Phys. Rev. C **95**, 031601(R) (2017).

[43] J. O. Newton, R. D. Butt, M. Dasgupta, D. J. Hinde, I. I. Gontchar, C. R. Morton, and K. Hagino, Phys. Rev. C **70**, 024605 (2004).

[44] L. R. Gasques, M. Evers, D. J. Hinde, M. Dasgupta, P. R. S. Gomes, R. M. Anjos, M. L. Brown, M. D. Rodriguez, R. G. Thomas, and K. Hagino, Phys. Rev. C **76**, 024612 (2007).

[45] D. J. Hinde, R. L. Ahlefeldt, R. G. Thomas, K. Hagino, M. L. Brown, M. Dasgupta, M. Evers, L. R. Gasques, and M. D. Rodriguez, Phys. Rev. C **76**, 014617 (2007).

[46] M. Evers, M. Dasgupta, D. J. Hinde, L. R. Gasques, M. L. Brown, R. Rafiei, and R. G. Thomas, Phys. Rev. C **78**, 034614 (2008).

[47] A. B. Balantekin and P. E. Reimer, Phys. Rev. C **33**, 379 (1986).

[48] A. B. Balantekin, A. J. DeWeerd, and S. Kuyucak, Phys. Rev. C **54**, 1853 (1996).

[49] A. Wakhle, C. Simenel, D. J. Hinde, M. Dasgupta, M. Evers, D. H. Luong, R. du Rietz, and E. Williams, Phys. Rev. Lett. **113**, 182502 (2014).

[50] A. S. Umar, V. E. Oberacker, and C. Simenel, Phys. Rev. C **94**, 024605 (2016).

[51] V. E. Oberacker, A. S. Umar, and C. Simenel, Phys. Rev. C **90**, 054605 (2014).

[52] V. I. Zagrebaev and W. Greiner, Phys. Rev. C **78**, 034610 (2008).

[53] K. Siwek-Wilczyńska, A. Borowiec, I. Skwira-Chalot, and J. Wilczyński, Int. J. Mod. Phys. E **17**, 12 (2008).

[54] R. Yanez, W. Loveland, J. S. Barrett, L. Yao, B. B. Back, S. Zhu, and T. L. Khoo, Phys. Rev. C **88**, 014606 (2013).

[55] R. du Rietz, D. J. Hinde, M. Dasgupta, R. G. Thomas, L. R. Gasques, M. Evers, N. Lobanov, and A. Wakhle, Phys. Rev. Lett. **106**, 052701 (2011).

[56] J. R. Leigh, M. Dasgupta, D. J. Hinde, J. C. Mein, C. R. Morton, R. C. Lemmon, J. P. Lestone, J. O. Newton, H. Timmers, J. X. Wei, and N. Rowley, Phys. Rev. C **52**, 3151 (1995).

[57] P. Moller, J. R. Nix, W. D. Myers, and W. J. Swiatecki, At. Data Nucl. Data Tables **59**, 185 (1995).

[58] R. H. Spear, At. Nucl. Data Tables **42**, 55 (1989).

[59] S. Raman, C. H. Malarkey, W. T. Milner, C. W. Nestor Jr., and P. H. Stelson, At. Data Nucl. Data Tables **36**, 1 (1987).